

Multiscale approximation and two-grid preconditioner for extremely anisotropic heat flow

Maria Vasilyeva^a, Golo Wimmer^b, Ben S. Southworth^b

^a*Department of Mathematics and Statistics, Texas A&M University - Corpus Christi, Corpus Christi, Texas, USA.*

^b*Theoretical Division, Los Alamos National Laboratory, P.O. Box 1663, Los Alamos, NM 87545 USA.*

Abstract

We consider anisotropic heat flow with extreme anisotropy, as arises in magnetized plasmas for fusion applications. Such problems pose significant challenges in both obtaining an accurate approximation as well in the construction of an efficient solver. In both cases, the underlying difficulty is in forming an accurate approximation of temperature fields that follow the direction of complex, non-grid-aligned magnetic fields. In this work, we construct a highly accurate coarse grid approximation using spectral multiscale basis functions based on local anisotropic normalized Laplacians. We show that the local generalized spectral problems yield local modes that align with magnetic fields, and provide an excellent coarse-grid approximation of the problem. We then utilize this spectral coarse space as an approximation in itself, and as the coarse-grid in a two-level spectral preconditioner. Numerical results are presented for several magnetic field distributions and anisotropy ratios up to 10^{12} , showing highly accurate results with a large system size reduction, and two-grid preconditioning that converges in $\mathcal{O}(1)$ iterations, independent of anisotropy.

Keywords: Anisotropic diffusion, generalized multiscale finite elements, two-grid preconditioner, magnetic confinement fusion

1. Introduction

In magnetic confinement fusion, heat is transported along magnetic field lines up to 10 orders of magnitude faster than across [26]. Together with typical time step sizes considered for magnetohydrodynamic (MHD) simulations, the corresponding extremely anisotropic diffusion equation poses numerical challenges both with respect to accuracy and solver efficiency. This holds true especially for scenarios in which the magnetic field topology is not aligned with the numerical mesh, which will generally be the case for more complex MHD simulations including magnetic islands and stochastic field configurations. In particular, low accuracy discretizations are typically characterized by numerical cross-diffusion of parallel heat flux in the perpendicular direction, leading to spuriously low confinement times.

To avoid this, higher-order approximations are often considered, e.g. [39]. A high-order interior penalty discontinuous Galerkin finite element scheme is presented in [25], and a hybridized discontinuous

*Corresponding author

Email addresses: maria.vasilyeva@tamucc.edu (Maria Vasilyeva), gwimmer@lanl.gov (Golo Wimmer), southworth@lanl.gov (Ben S. Southworth)

Galerkin scheme is considered in [24]. In [26], a finite element analog to the second-order, finite difference scheme for the solution of the anisotropic diffusion equation in strongly magnetized plasmas is presented with a fourth-order extension. Other approaches include mixed Virtual Element Methods as considered in [6], and nonlinear constrained finite element approximations in [27]. Due to the highly directional nature of problems with extreme anisotropy ratios, as well as the effective decoupling of solutions on different field lines, techniques from discretizing hyperbolic equations have also proven useful. In [37], the authors show that standard algorithms for anisotropic diffusion based on centered differencing do not preserve monotonicity and can lead to the violation of the entropy constraints of the second law of thermodynamics. To solve these problems, algorithms based on slope limiters, analogous to those used in second-order schemes for hyperbolic equations, are proposed. A high-order finite difference solver for anisotropic diffusion problems based on the first-order hyperbolic system method is presented in [10]. More recently, we derived discontinuous [50] and continuous Galerkin [51] finite element formulations based on a certain mixed formulation, incorporating stabilization techniques used in hyperbolic equations for directional gradients.

For general meshes and implicit time integration, fast linear solvers also pose a major challenge for extreme levels of anisotropy. For high-performance simulations, ideally one would use multilevel methods. However, geometric multigrid methods require some combination of line/plane relaxation and semi-coarsening [40, 9], which is expensive, difficult to realize in parallel, and limited to structured grids. Algebraic multigrid (AMG) methods can automatically semi-coarsen in non-grid-aligned directions (e.g., see [38, Fig. 3]), and specialized AMG methods have been developed for anisotropic diffusion, e.g. [36, 30, 22, 7], but we have found that these methods still fail on realistic non-grid-aligned anisotropies (e.g., [50]). In [50] we develop a specialized mixed discretization and block preconditioner for highly anisotropic diffusion built on AMG for hyperbolic transport operators [31, 29], but the solver studies therein are limited to open (i.e. acyclic) field lines, which is not realistic in many practical fusion settings.

In order to reduce the size of the system and construct a computationally efficient solver, we propose a coarse grid approximation built on spectral multiscale basis functions. The concept of using local spectral problems to accurately approximate highly heterogeneous media was proposed in the Generalized Multiscale Finite Element Method (GMsFEM) [19, 17]. Later, this method was applied to many different applications, such as transport and flow problems, poroelasticity problems in heterogeneous and fractured media, electro-chemical processes in Lithium-Ion Batteries, geothermal research simulations and seismic wave propagations [16, 45, 2, 43, 42, 44]. Recently, we adapted the spectral multiscale approach to a general class of discrete problems described using the graph Laplacian [41, 46]. The proposed approach is based on spectral characteristics of the normalized local graph Laplacian. The central idea of the GMsFEM was associated with a multicontinuum approach and used to construct a nonlocal multicontinuum upscaling (NLMC) [13, 14]. The NLMC is based on constrained energy minimization and provides a good approximation on a coarse grid with sufficient oversampling layers in the basis construction. Moreover, it has been shown that constructing a prolongation operator based on the solution of the local spectral problems gives a basis for constructing highly efficient preconditioners in the spectral algebraic multigrid method [11, 20, 8, 21, 18]. Most traditional approaches in multiscale model order reduction address highly varied properties in a classic manner related to heterogeneous properties, but do not explore high-contrast variations caused by physical fields that span the entire domain. Some work in element-based AMG has been successfully applied to anisotropic diffusion, e.g. [12], but the problems considered have sufficiently mild anisotropy that existing AMG solvers (i.e., without spectral coarse modes), e.g. [30, 36, 22, 7], can still be effective solvers. In this work, we address the construct associated with the two heat flow directions: parallel and perpendicular. As mentioned earlier, in real applications, the ratio between parallel and perpendicular heat conductivities can reach 10^{10} or higher, and the main challenge is associated with

the parallel direction of heat flow following the magnetic field, particularly for non-grid-aligned meshes.

In this work, we show that the local generalized spectral problems applied to the anisotropic diffusion equation yield eigenfunctions that align with the magnetic field lines and give a very good approximation of the problem on a coarse grid. Thus, even without enforcing mesh alignment with a given magnetic field, we are able to integrate in a basis that effectively *does* respect the magnetic field structure. More specifically, we start with a finite element approximation on a sufficiently fine grid with second-order polynomial basis functions, and use this as a reference solution to estimate the accuracy of the proposed coarse grid approximation. We then construct a highly accurate approximation by introducing a local generalized eigenvalue problem and use eigenvectors associated with the smallest eigenvalues to construct a multiscale space aligned with a magnetic field-directed heat flux. We show approximation properties of the constructed multiscale space, and then incorporate the coarse multiscale space into a two-grid preconditioner. Multiscale approximation results are used to prove convergence of the two-grid method, independent of anisotropy. We present numerical accuracy investigations for three test problems with different magnetic fields and varying contrasts of parallel and perpendicular heat conductance. We show that with sufficiently many multiscale basis functions, we can obtain highly accurate results with a large system size reduction, and in the context of a two-grid preconditioner, achieve convergence in $\mathcal{O}(1)$ iterations, independent of anisotropy.

The paper is structured as follows. In Section 2, we outline the problem formulation for anisotropic diffusion, presenting weak formulations and approximations on a fine grid. Section 3 presents a coarse grid approximation using a spectral multiscale space and discusses approximation properties of the proposed multiscale method. A two-grid method built around the spectral multiscale coarse space is discussed in Section 4, including a proof of two-grid convergence. Numerical results are presented in Section 5 to illustrate the robustness and accuracy of the proposed method for three test cases with different magnetic field setups. We show that the method provides an accurate approximation given a sufficient number of multiscale basis functions and coarse grid size. The paper ends with a conclusion.

2. Problem formulation

We consider anisotropic diffusion in a domain Ω for temperature $T = T(t, x)$:

$$T_t - \nabla \cdot \mathbf{q} = f, \quad x \in \Omega, \quad t > 0, \quad (1)$$

with

$$\mathbf{q} = k_{\parallel} \nabla_{\parallel} T + k_{\perp} \nabla_{\perp} T, \quad \nabla_{\parallel}(\cdot) = (\mathbf{b} \cdot \nabla(\cdot))\mathbf{b}, \quad \nabla_{\perp} = \nabla - \nabla_{\parallel}, \quad (2)$$

with given initial conditions $T(0, x) = T_0$ for $x \in \Omega$ and Dirichlet boundary conditions

$$T(t, x) = g, \quad x \in \partial\Omega, \quad t > 0.$$

Here $\mathbf{b} = \mathbf{B}/|\mathbf{B}|$, where \mathbf{B} is the given magnetic field, and k_{\parallel} and k_{\perp} are the heat conductivity parallel and perpendicular to normalized magnetic field lines \mathbf{b} , respectively.

Substituting (2) to (1), we obtain the following formulation:

$$T_t - \nabla \cdot (k_{\perp} \nabla T) - \nabla \cdot (k_{\Delta} \mathbf{b}(\mathbf{b} \cdot \nabla T)) = f, \quad (3)$$

with $k_{\Delta} = k_{\parallel} - k_{\perp}$.

Let $V = \{v \in H^1(\Omega) : v = g \text{ on } \partial\Omega\}$ and $\hat{V} = \{v \in H^1(\Omega) : v = 0 \text{ on } \partial\Omega\}$. Then, we can write the following variational formulation: find $T \in V$ such that

$$m(T_t, v) + a(T, v) = l(v), \quad \forall v \in \hat{V}, \quad (4)$$

with

$$\begin{aligned} a(T, v) &= a_{iso}(T, v) + a_{aniso}(T, v), \quad m(T, v) = \int_{\Omega} T v \, dx, \quad l(f) = \int_{\Omega} f v \, dx, \\ a_{iso}(T, v) &= \int_{\Omega} k_{\perp} \nabla T \cdot \nabla v \, dx, \quad a_{aniso}(T, v) = \int_{\Omega} k_{\Delta} (\mathbf{b} \cdot \nabla T) (\mathbf{b} \cdot \nabla v) \, dx. \end{aligned} \quad (5)$$

Let \mathcal{T}_h be a finite element partition of the domain into elements K_i with mesh size h

$$\mathcal{T}_h = \cup_{i=1}^{N_h^{cell}} K_i,$$

where N_h^{cell} is the number of cells. We call \mathcal{T}_h a “fine grid,” where we assume the fine grid has sufficient resolution of the magnetic field \mathbf{b} and temperature field T that it can provide an accurate approximate solution using standard polynomial basis functions. For approximation space on the fine grid \mathcal{T}_h , we use a continuous Galerkin (CG) formulation. The variational problem reads: find $T \in V_h \subset V$ such that

$$m((T_h)_t, v) + a(T_h, v) = l(v), \quad \forall v \in \hat{V}_h \subset \hat{V}, \quad (6)$$

where

$$T_h = \sum_{j=1}^{N_h} T_j \phi_j(x), \quad V_h = \text{span}\{\phi_j, j = 1, \dots, N_h\}.$$

Let τ be the time step size and T_h^n be the solution at time t^n . Then, using a backward Euler time approximation, we obtain the following discrete problem: find $T_h^n \in V_h$ such that

$$\frac{1}{\tau} m(T_h^n, v) + a(T_h^n, v) = \frac{1}{\tau} m(T_h^{n-1}, v) + l(v), \quad \forall v \in \hat{V}. \quad (7)$$

Note, this form generalizes to implicit multistage or multistep methods as well, with a modified linear forcing function. Altogether, we arrive at a discrete problem for each implicit time step (7) in the following matrix form

$$\left(\frac{1}{\tau} M_h + A_h \right) T_h^n = \frac{1}{\tau} M_h T_h^{n-1} + F_h, \quad (8)$$

where $M_h = \{m_{ij} = m(\phi_i, \phi_j)\}$, $A_h = \{a_{ij} = a(\phi_i, \phi_j)\}$ and $F_h = \{f_j = l(\phi_j)\}$.

3. Multiscale space approximation

Let \mathcal{T}_H be a finite element partition of the domain and mesh into coarse elements $\{K_i\}$ with mesh size $H \gg h$:

$$\mathcal{T}_H = \cup_{i=1}^{N_H^{cell}} K_i,$$

where N_H^{cell} is the number of coarse cells (left plot in Figure 1). We then consider a CG formulation for a coarse grid approximation as well, and construct nodal multiscale basis functions for the coarse variational problem.

For nodal basis functions, let ω_i be the subdomain defined as the collection of coarse cells containing coarse grid node x_i . Let $\mathcal{T}_h^{\omega_i}$ be the fine-scale partitioning of the local domain ω_i . We suppose that $\mathcal{T}_h^{\omega_i}$ is conforming with global finite element partitioning \mathcal{T}_h , so we are able to build a local-to-global map for all local degrees of freedom $DOF_h^{\omega_i} = N_h^{\omega_i}$ to global $DOF_h = N_h$. In addition, we define a partition of unity function χ_i defined in ω_i . This approach will use a regular bilinear partition of unity functions (right plot in Figure 1).

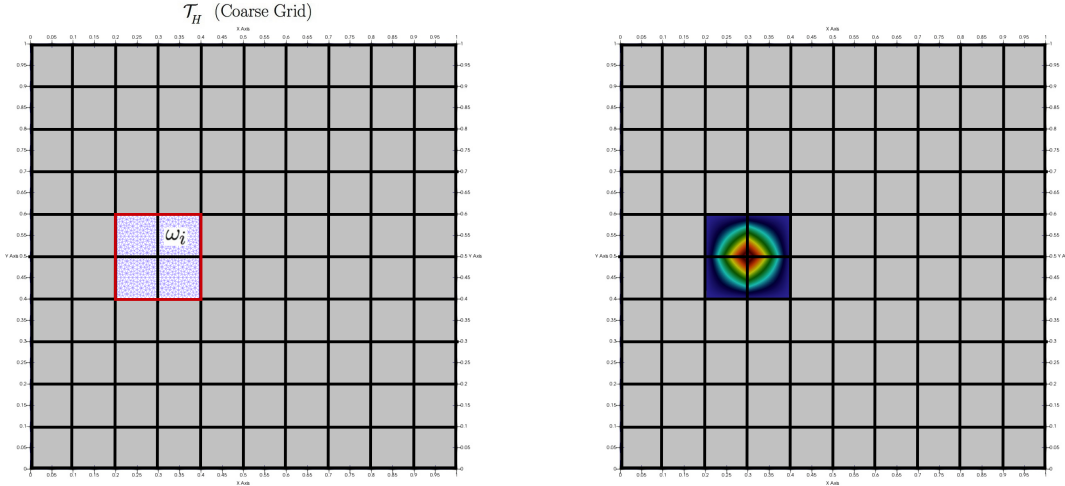


Figure 1: Illustration of the 10×10 coarse grid \mathcal{T}_H with local domain ω_i and linear partition of unity function χ_i

For the construction of a basis that provides an accurate approximation on the coarse grid \mathcal{T}_H , we will construct spectral multiscale basis functions motivated by the Generalized Multiscale Finite Element Method (GMsFEM) [19, 17, 15]. In the presented approach, we design an eigenvalue problem based on the normalized anisotropic Laplacian operator recently presented for a general class of problems on graph [41]. We introduce a local spectral problem in each local domain ω_i and show that the eigenvectors naturally follow the underlying magnetic field lines, and can provide superior approximation for the considered problem compared with typical piecewise polynomials.

Assuming a fixed in time magnetic field, the algorithm for the multiscale method contains offline and online stages:

- *Offline calculations.*
 - Define coarse grid \mathcal{T}_H and generate local domains ω_i .
 - Solve local spectral problems to construct a set of multiscale basis functions $\{\psi_j^{\omega_i}\}$ in each local domain ω_i independently.
 - Map the local degrees of freedom to global and form an interpolation operator P using a given number of J local multiscale basis functions over each subdomain, where

$$P = \left[\psi_1^{\omega_1}, \dots, \psi_J^{\omega_1}, \dots, \psi_1^{\omega_{N_H^{vert}}}, \dots, \psi_J^{\omega_{N_H^{vert}}} \right].$$

- *Online calculations.*

- Project matrices and vectors to the coarse grid using the precomputed interpolation matrix P and restriction matrix $R = P^T$.
- Solve the coarse-scale system.
- Interpolate the coarse-scale solution to the fine grid resolution.

Next, we describe the construction of the spectral multiscale basis functions and discuss approximation properties of the multiscale space.

3.1. Spectral multiscale basis functions

Within the fine grid resolution of the local domain ω_i , we solve the following generalized eigenvalue problem in matrix form

$$A_h^{\omega_i} \phi^{\omega_i} = \lambda D_h^{\omega_i} \phi^{\omega_i}, \quad (9)$$

where

$$A_h^{\omega_i} = \{a_{ij}^{\omega_i} = a^{\omega_i}(\phi_i, \phi_j)\}, \quad a^{\omega_i}(u, v) = a_{iso}^{\omega_i}(u, v) + a_{aniso}^{\omega_i}(u, v),$$

$$a_{iso}^{\omega_i}(u, v) = \int_{\omega_i} k_{\perp} \nabla u \cdot \nabla v \, dx, \quad a_{aniso}^{\omega_i}(u, v) = \int_{\omega_i} k_{\Delta} (b \cdot \nabla u)(b \cdot \nabla v) \, dx,$$

and $D_h^{\omega_i} = \text{diag}(d_1^{\omega_i}, \dots, d_{N_h^{\omega_i}}^{\omega_i})$, where $d_i^{\omega_i} = a_{ii}^{\omega_i}$ are the diagonal elements of the matrix $A_h^{\omega_i}$ [41, 11, 20, 8]. Here $A_h^{\omega_i}$ and $D_h^{\omega_i}$ are assumed to be SSPD by nature of the underlying problem and discretization, implying the generalized eigenvalues are real and nonnegative, and the eigenvectors form an orthogonal basis. Moreover, the first eigenvalue is zero with a constant corresponding eigenvector, as only natural boundary conditions are imposed on the local bilinear form.

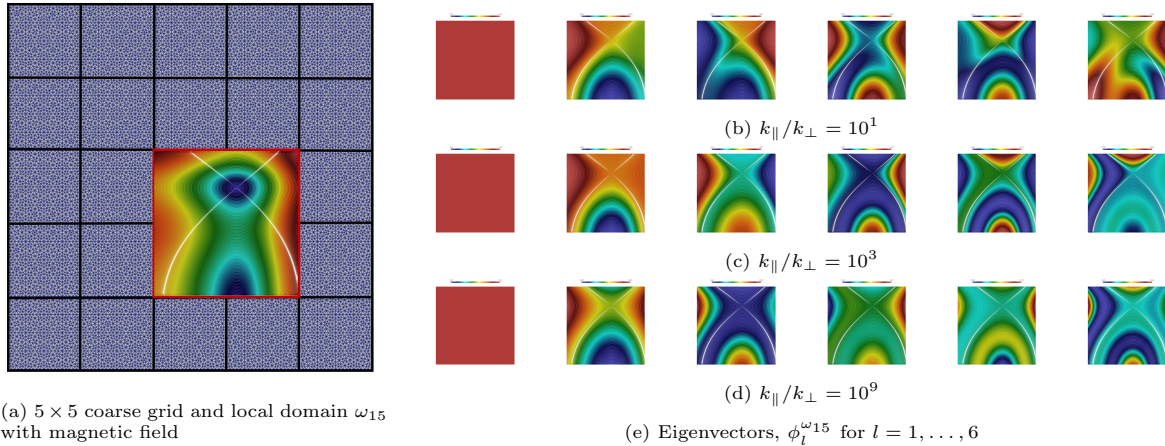


Figure 2: Local domain with magnetic field and corresponding eigenvectors for three different anisotropy ratios.

In order to choose the most “meaningful” eigenvectors, we order eigenvalues $\{\lambda_j\}$ in increasing magnitude $\lambda_1 \leq \lambda_2 \leq \dots \leq \lambda_j \leq \dots$ with corresponding eigenvectors $\{\phi_j^{\omega_i}\}$. The spectral multiscale basis functions with the smallest eigenvalues follow heat flow in the direction of the magnetic field, as represented in Figure 2. We plot the first six eigenvectors in the local domain ω_{15} on a 5×5 coarse grid for three anisotropy ratios $k_{\parallel}/k_{\perp} = 10^1, 10^3$ and 10^9 . The first eigenvector is constant or near constant

(to remove unnecessary oscillations, we artificially make the first basis constant in the presence of small oscillations). From the next five eigenvectors, we observe how the anisotropy ratio affects them. For small anisotropy, the basis functions largely respect the magnetic field lines in the parallel direction, but the perpendicular diffusion must also be accounted for, and we can see that the basis functions also represent heat flow in that direction. In contrast, for high anisotropy we observe that eigenvectors are more or less exclusively aligned with the magnetic field lines, only representing heat flow in the parallel direction.

3.2. Coarse grid approximation

We choose eigenvectors corresponding to the J^{ω_i} smallest eigenvalues and define a multiscale space

$$V_H = \text{span}\{\psi_j^{\omega_i} = \chi_i \phi_j^{\omega_i}, j = 1, \dots, J^{\omega_i}, i = 1, \dots, N_H^{\text{vert}}\},$$

where χ_i is the linear partition of unity functions and N_H^{vert} is the number of local domains (number of coarse grid vertices).

The multiscale solution $T_{ms} \in V_H$ can be obtained as follows

$$\frac{1}{\tau} m(T_{ms}^n - T_{ms}^{n-1}, v) + a(T_{ms}^n, v) = l(v), \quad \forall v \in V_H, \quad (10)$$

where $T_{ms}^n = \sum_{i=1}^{N_H^{\text{vert}}} \sum_{j=1}^{J^{\omega_i}} T_{i,j}^n \psi_j^{\omega_i}$.

From an implementation perspective, we create an interpolation operator from the coarse to the fine grid (P) and Galerkin restriction operator from the fine to the coarse grid ($R = P^T$), where

$$P = \left[\psi_1^{\omega_1}, \dots, \psi_{J^{\omega_1}}^{\omega_1} \dots \psi_1^{\omega_{N_H^{\text{vert}}}}, \dots, \psi_{J^{\omega_{N_H^{\text{vert}}}}}^{\omega_{N_H^{\text{vert}}} \right]. \quad (11)$$

where the spectral multiscale basis functions $\psi_j^{\omega_i}$ are mapped from local indexing in $\mathcal{T}_h^{\omega_i}$ to global indexing in \mathcal{T}_h .

On the coarse grid we then have the following reduced order implicit equation:

$$\frac{1}{\tau} M_H T_H^n + A_H T_H^n = \frac{1}{\tau} M_H T_H^{n-1} + F_H, \quad (12)$$

with

$$M_H = P^T M_h P, \quad A_H = P^T A_h P, \quad F_H = P^T F_h,$$

where T_H^n is the solution on the coarse grid at time t_n . The fine-scale solution is reconstructed by

$$T_{ms}^n = P T_H^n.$$

The size of the coarse equation (12) is $DOF_H = \sum_{i=1}^{N_H^{\text{vert}}} J^{\omega_i}$, with J^{ω_i} denoting the number of local multiscale basis functions in ω_i . In our numerical approach, we take the same number of basis functions in each local domain ω_i ($J^{\omega_i} = J$), then $DOF_H = J \cdot N_H^{\text{vert}}$.

3.3. Convergence of the multiscale space

In this section, we analyze the convergence of the multiscale space induced by a generalized spectral problem (9) to understand how the number of multiscale basis functions and coarse grid resolution affect the coarse grid approximation error. We consider the following norms [1, 19, 41]

$$\begin{aligned} \|u\|_{D_h}^2 &= u^T D_h u = (u, u)_{D_h}, & \|u\|_{A_h}^2 &= u^T A_h u = (u, u)_{A_h}, \\ \|B_h u\|_{D_h}^2 &= (B_h u)^T D_h (B_h u) = (A_h u)^T D_h^{-1} (A_h u) = (B_h u, B_h u)_{D_h} = (A_h u, A_h u)_{D_h^{-1}}, \end{aligned}$$

with $B_h = D_h^{-1}A_h$, $D_h = D_h^T > 0$ and $A_h = A_h^T > 0$.

To construct spectral multiscale basis functions, we solve a generalized eigenvalue problem (9) in each subdomain ω_i and choose eigenvectors $\phi_j^{\omega_i}$ ($j = 1, \dots, J^{\omega_i}$) corresponding to the J^{ω_i} smallest eigenvalues $\lambda_j^{\omega_i}$. The eigenvectors $\{\phi_j^{\omega_i}\}$ form an orthonormal basis with respect to the inner product $(u, v)_{D_h^{\omega_i}}$. Then, in each local domain ω_i , we define the local projection as follows

$$P_{J^{\omega_i}}^{\omega_i} v = \sum_{j=1}^{J^{\omega_i}} (v, \phi_j^{\omega_i})_{D_h^{\omega_i}} \phi_j^{\omega_i}, \quad v \in V_h. \quad (13)$$

For the local projection the following inequalities hold (see [1] for details):

$$\begin{aligned} \|v - P_{J^{\omega_i}}^{\omega_i} v\|_{D_h^{\omega_i}}^2 &\leq \frac{1}{\lambda_{J^{\omega_i}+1}^{\omega_i}} \|v\|_{A_h^{\omega_i}}^2, \quad \|v - P_{J^{\omega_i}}^{\omega_i} v\|_{A_h^{\omega_i}}^2 \leq \frac{1}{\lambda_{J^{\omega_i}+1}^{\omega_i}} \|B_h^{\omega_i} v\|_{D_h^{\omega_i}}^2, \\ \|v - P_{J^{\omega_i}}^{\omega_i} v\|_{D_h^{\omega_i}}^2 &\leq \frac{1}{(\lambda_{J^{\omega_i}+1}^{\omega_i})^2} \|B_h^{\omega_i} v\|_{D_h^{\omega_i}}^2. \end{aligned} \quad (14)$$

The first inequality corresponds to a local weak approximation property over ω_i in multigrid literature [47]. Assuming unit diagonal so that $D_h^{\omega_i} = I$, the second inequality corresponds to a local strong approximation property [47], and the third a local fractional approximation property FAP(1,0) [32, Def. 1] (these latter approximation properties are not generalized in multigrid literature to $D_h^{\omega_i} \neq I$).

Next, we write the coarse interpolation $\Pi: V_h \rightarrow V_H$ as follows

$$\Pi v = \sum_{i=1}^{N_H^{vert}} \chi_i (P_{J^{\omega_i}}^{\omega_i} v). \quad (15)$$

and $v - \Pi v = \sum_{i=1}^N \chi_i (v - P_{J^{\omega_i}}^{\omega_i} v)$. Using properties of partition of unity functions χ_i ($\chi_i \leq 1$ and $|\nabla \chi_i| \leq 1/H^2$) [33], we can obtain the following estimates for the global projection

$$\begin{aligned} \|u - \Pi u\|_{D_h}^2 &= \sum_K \|u - \Pi u\|_{D_h^K}^2 \\ &\leq \sum_K \sum_{x_l \in K} \|\chi_l (u - P_{J^{\omega_l}}^{\omega_l} u)\|_{D_h^{\omega_l}}^2 \leq \sum_K \sum_{x_l \in K} \|u - P_{J^{\omega_l}}^{\omega_l} u\|_{D_h^{\omega_l}}^2, \\ \|u - \Pi u\|_{A_h}^2 &\leq \sum_K \sum_{x_l \in K} \|\chi_l (u - P_{J^{\omega_l}}^{\omega_l} u)\|_{A_h^{\omega_l}}^2 \\ &\leq \sum_K \sum_{x_l \in K} \frac{1}{H^2} \|u - P_{J^{\omega_l}}^{\omega_l} u\|_{D_h^{\omega_l}}^2 + \sum_K \sum_{x_l \in K} \|u - P_{J^{\omega_l}}^{\omega_l} u\|_{A_h^{\omega_l}}^2. \end{aligned}$$

We let $\lambda_{J+1} = \min_K \lambda_{K,J+1}$ and $\lambda_{K,J+1} = \min_{x_l \in K} \lambda_{J^{\omega_l}+1}^{\omega_l}$, therefore by combing with estimates for local projection (14) we obtain

$$\begin{aligned} \|v - \Pi v\|_{D_h}^2 &\leq \frac{1}{\lambda_{J+1}} \|v\|_{A_h}^2, \\ \|v - \Pi v\|_{A_h}^2 &\leq \left(\frac{1}{H^2 \lambda_{J+1}^2} + \frac{1}{\lambda_{J+1}} \right) \|B_h v\|_{D_h}^2, \\ \|v - \Pi v\|_{D_h}^2 &\leq \frac{1}{\lambda_{J+1}^2} \|B_h v\|_{D_h}^2. \end{aligned} \quad (16)$$

Here we have that Π satisfies weak, strong, and fractional FAP(1, 0) approximation properties, respectively, with constants as shown above. As discussed in Appendix B, the weak approximation property provides necessary and sufficient conditions for convergence of a two-grid method.

Finally under some additional regularity and appropriate initial conditions, we have the following error estimate of the multiscale method (see Appendix A)

$$\|T_h^n - T_{ms}^n\|_{M_h}^2 + \tau \sum_{k=1}^n \|T_h^k - T_{ms}^k\|_{A_h}^2 \leq \|T_h^0 - T_{ms}^0\|_{M_h}^2 + \tau \sum_{k=1}^n \frac{H^2}{\Lambda^*} \|B_h T_h^k\|_{D_h}^2, \quad (17)$$

where $\Lambda^* = \lambda_{J+1} H^2$ (local domain is scaled to a domain of size one), $T_h^n \in V_h$ and $T_{ms}^n \in V_H$ are the fine-scale and multiscale solutions from (7) and (10), respectively.

4. Two-grid multiscale preconditioner

Next, we consider the construction of the iterative solver, where we use the constructed multiscale space as a two-grid preconditioner that converges independently of the contrast of the parallel and perpendicular heat conductivities. Such contrast is challenging for a typical multigrid preconditioner. In contrast with classic geometric or algebraic restriction and interpolation operators, our transfer operators built on local spectral problems lead to a very accurate coarse approximation, as shown above.

Following equation (8), for each implicit time step we solve a system of linear equations

$$Q_h T_h^n = b_h^{n-1}, \quad (18)$$

where

$$Q_h = \frac{1}{\tau} M_h + A_h, \quad b_h^{n-1} = \frac{1}{\tau} M_h T_h^{n-1} + F_h.$$

Following equation (12), we have the following system on the coarse grid

$$Q_H T_H^n = b_H^{n-1}, \quad T_{ms}^n = P T_H^n, \quad (19)$$

where

$$Q_H = \frac{1}{\tau} M_H + A_H, \quad b_H^{n-1} = \frac{1}{\tau} M_H T_H^{n-1} + F_H.$$

Next, we follow the framework of the Algebraic Multigrid Method (AMG) method in constructing a two-grid solver [35, 53, 47, 20, 48]. For a given initial guess $y_h^{(0)} = T_h^{n-1}$ in the two-grid algorithm and smoothing operator $S \approx Q_h$, we have:

1. *Pre-smoothing:*

$$y_h^{(1)} = y_h^{(0)} + S^{-1} r_h^{(0)}, \quad r_h^{(0)} = (b_h^{n-1} - Q_h y_h^{(0)})$$

2. *Coarse-grid correction:*

2.1 *Restriction:*

$$r_H = P^T r_h^{(1)}, \quad r_h^{(1)} = (b_h^{n-1} - Q_h y_h^{(1)}).$$

2.2 *Coarse-grid solution:*

$$Q_H e_H = r_H.$$

2.3 *Interpolation and update:*

$$y^{(2)} = y^{(1)} + P e_H.$$

3. *Post-smoothing*:

$$y_{TG} = y^{(2)} + S^{-T} r_h^{(2)}, \quad r_h^{(2)} = (b_h^{n-1} - Q_h y_h^{(2)}).$$

In the two-grid algorithm, we have the following error transfer operator [20, 34]

$$E_{TG} = (I - S^{-T} Q_h)(I - P Q_H^{-1} P^T Q_h)(I - S^{-1} Q_h).$$

In this work, we use five pointwise Jacobi and symmetric Gauss-Seidel iteration pre- and post-smoothing iterations to remove high-frequency errors. A multiscale coarse-grid correction is used to attenuate the remaining error not effectively reduced by smoothing.

The two-grid error propagation can be expressed as follows [20, 47]

$$E_{TG} = I - C_{TG}^{-1} Q_h,$$

with

$$C_{TG}^{-1} = \bar{S}^{-1} + (I - S^{-T} Q_h) P Q_H^{-1} P^T (I - Q_h S^{-1}),$$

where $\bar{S} = S(S + S^T - Q_h)^{-1} S^T$ is the so-called symmetric smoother.

For the method's convergence, we have [47, 8, 20]

$$0 \leq v^T Q_h E_{TG} v \leq \left(1 - \frac{1}{K_{TG}}\right) v^T Q_h v,$$

with

$$v^T Q_h v \leq v^T C_{TG} v \leq K_{TG} v^T Q_h v, \quad \text{where } K_{TG} := \text{Cond}(C_{TG}^{-1} Q_h).$$

Using properties of the Jacobi and Gauss-Seidel smoothers, spectral equivalence to the diagonal part of the matrix Q_h , and approximation properties of the spectral multiscale space discussed in the previous section, we obtain (see Appendix B for details)

$$K_{TG} = \left(1 + \frac{C}{\tau}\right) \frac{H^2}{\Lambda^*}.$$

Therefore, given a sufficient number of multiscale basis functions, we can obtain anisotropy-independent convergence of the iterative solver. More importantly, in Section 5.2 we show that $\mathcal{O}(1)$ local basis functions are sufficient for robust anisotropy-independent convergence.

5. Numerical results

We consider anisotropic heat flow in a square domain $\Omega = [0, 1]^2$, with $\kappa_{\perp} = 1$ and $\kappa_{\parallel} \gg 1$ such that the ratio $\kappa_{\perp}/\kappa_{\parallel}$ ranges from 10^3 to 10^{12} . We simulate with $t_{max} = 5 \cdot 10^{-6}$ using 10 time steps. Note, the time step is fixed for all anisotropies, which makes for a relatively small timestep at the smallest anisotropy, but a large time step and very stiff system for the largest anisotropy ratio. Although the focus of this paper is on spatial discretization, for realistically high anisotropy ratios a steady formulation of the problem is extremely ill conditioned/bordering on ill-posed, hence why we consider a short time evolution formulation to test the multiscale spatial representation and preconditioner. The fine grid contains 100,292 triangular cells, 150,838 facets and 50,547 vertices. The fine grid solution using a CG FEM approximation with P^2 elements is used as a reference solution. Then the number of unknowns of

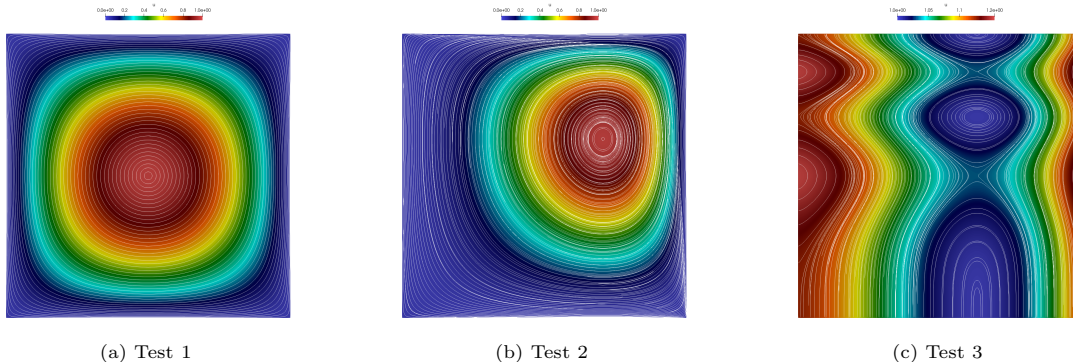


Figure 3: Reference solutions with magnetic field lines at final time for Test 1, 2 and 3, $DOF_h = 201,385$

the fine grid problem is $DOF_h = N_h = N_h^{vert} + N_h^e = 201,385$, where N_h^{vert} is the number of fine grid vertices and N_h^e is the number of fine grid facets.

We simulate three test cases represented in Figure 3. Each case is characterized by a given magnetic field (Test 1, 2, and 3). In Figure 3, we plot the temperature distribution with magnetic field lines depicted in white lines. We set a source term $f = \kappa_{\perp} \Delta T_0$ that simulates a counter-forcing. The implementation is based on the FEniCS library [28]. To solve the spectral problem for the multiscale basis functions construction, we use the sparse package from scipy [49]. The Gmsh library [23] is used to construct a fine-grid conformed with coarse grid edges.

5.1. Multiscale space approximation

To investigate the accuracy of the proposed multiscale method, we consider 10×10 and 20×20 coarse grids. The size of the resulting coarse-grid system is $DOF_H = \sum_{i=1}^{N_H^{vert}} J^{\omega_i}$, with J^{ω_i} denoting the number of local multiscale basis functions in ω_i . In our numerical approach, we take the same number of basis functions in each local domain ω_i ($J^{\omega_i} = J$), then $DOF_H = J \cdot N_H^{vert}$. Then we have $DOF_H = J \cdot 121$ for the 10×10 coarse grid and $DOF_H = J \cdot 441$ for the 20×20 coarse grid. We use a direct solver with LU factorization for coarse-scale approximations.

For error calculations, we use the relative L_2 error for the temperature field at the final time

$$err = \frac{\|T_h - T_{ms}\|_{L_2}}{\|T_h\|_{L_2}},$$

where $\|u\|_{L_2}^2 = u^T u = (u, u)$.

Tables 1, 2, and 3 contain numerical results for the presented multiscale method for Tests 1, 2, and 3, respectively. We investigate the influence of increasing the anisotropy ratio k_{\parallel}/k_{\perp} on the method's robustness, and also present errors within an increasing number of multiscale basis functions J , corresponding to the size of the coarse grid system DOF_H . The numerical results are presented for 10×10 and 20×20 coarse grids. The solution time is measured without taking into account the time it takes to construct the multiscale basis functions (restriction operator), which can be done in the offline stage. Therefore, the time indicated (denoted as tm_s) refers to the time required for online computations. It is worth noting that the offline stage of constructing the multiscale basis can be carried out in a fully parallel manner. Additionally, the computation time of the basis in a local domain depends on the size of

J	DOF_H	err 10^3	tm_s	err 10^6	tm_s	err 10^9	tm_s	err 10^{12}	tm_s
Coarse grid, 10×10									
1	121	5.53e-03	0.020	2.77e-01	0.020	1.00e+00	0.020	1.00e+00	0.020
2	242	6.59e-03	0.036	8.25e-02	0.037	2.34e-01	0.037	1.00e+00	0.037
3	363	2.84e-03	0.053	3.02e-02	0.054	5.22e-02	0.054	9.02e-01	0.054
4	484	1.53e-03	0.071	4.58e-03	0.073	6.28e-03	0.073	3.43e-01	0.072
6	726	6.57e-04	0.106	2.76e-03	0.106	9.70e-04	0.105	1.00e-02	0.106
8	968	2.78e-04	0.140	3.11e-04	0.140	2.69e-04	0.141	4.47e-03	0.143
12	1452	1.20e-04	0.211	3.07e-05	0.210	2.08e-05	0.211	4.26e-04	0.213
16	1936	5.72e-05	0.283	4.15e-06	0.281	9.49e-06	0.281	2.08e-04	0.284
24	2904	3.56e-05	0.426	4.51e-07	0.427	2.81e-06	0.427	4.79e-04	0.434
32	3872	2.97e-05	0.576	3.96e-07	0.573	2.68e-06	0.576	3.69e-04	0.579
40	4840	1.87e-05	0.725	4.18e-07	0.726	2.61e-06	0.730	3.82e-04	0.731
48	5808	1.37e-05	0.890	4.15e-07	0.887	2.40e-06	0.892	2.32e-04	0.892
56	6776	9.48e-06	1.048	3.95e-07	1.049	2.20e-06	1.055	2.11e-04	1.049
64	7744	6.24e-06	1.254	3.25e-07	1.219	2.16e-06	1.217	1.90e-04	1.218
Coarse grid, 20×20									
1	441	1.48e-03	0.018	1.23e-01	0.018	1.00e+00	0.019	1.00e+00	0.018
2	882	2.12e-03	0.033	4.21e-02	0.034	4.64e-01	0.033	1.00e+00	0.034
3	1323	1.24e-03	0.050	2.18e-02	0.049	4.10e-02	0.049	8.91e-01	0.050
4	1764	5.09e-04	0.065	8.45e-04	0.065	1.78e-03	0.065	5.32e-02	0.066
6	2646	3.57e-04	0.098	1.72e-04	0.098	1.07e-04	0.098	6.17e-03	0.099
8	3528	1.14e-04	0.131	2.64e-05	0.132	2.07e-05	0.131	1.46e-03	0.133
12	5292	3.42e-05	0.203	1.09e-06	0.200	2.09e-06	0.203	2.80e-04	0.203
16	7056	1.72e-05	0.278	3.84e-07	0.278	1.94e-06	0.280	2.15e-04	0.281
24	10584	5.51e-06	0.446	2.68e-07	0.446	1.48e-06	0.446	1.72e-04	0.447
32	14112	3.63e-06	0.641	3.31e-08	0.639	5.29e-07	0.642	5.85e-05	0.644
40	17640	1.88e-06	0.856	3.16e-08	0.854	5.35e-07	0.860	2.62e-04	0.858
48	21168	1.16e-06	1.108	2.20e-08	1.089	3.96e-07	1.101	5.52e-05	1.096
56	24696	7.97e-07	1.361	1.90e-08	1.361	5.09e-07	1.368	1.03e-04	1.352
64	28224	5.91e-07	1.648	4.32e-09	1.636	5.96e-07	1.665	1.28e-04	1.657

Table 1: Test 1. Relative L_2 error (err) with time of solution (tm_s)

the coarse grid, so it is important to find a balance between the coarse grid size and fine grid resolution in order to achieve faster calculations in the local domain.

Figure 4 illustrates the results presented in Tables 1, 2, and 3. The graph shows how the relative L_2 error decreases with respect to the size of the coarse grid system, DOF_H , to demonstrate the relationship between the number of basis functions M and the coarse grid resolution H . Generally, the error increases as J and coarse grid resolution increases in all test cases with four contrasts. The number of basis functions directly affects the system size, and therefore, the solution time is increased proportionally. We observe that higher anisotropy requires a larger number of basis functions to capture the fine-scale behavior. We also see that on the 20×20 coarse grid, we can obtain good results with a smaller number

J	DOF_H	err 10^3	tm_s	err 10^6	tm_s	err 10^9	tm_s	err 10^{12}	tm_s
Coarse grid, 10×10									
1	121	1.24e-02	0.019	5.57e-01	0.020	1.00e+00	0.019	1.00e+00	0.020
2	242	1.02e-02	0.037	1.08e-01	0.037	9.91e-01	0.038	1.00e+00	0.037
3	363	5.03e-03	0.054	4.23e-02	0.056	5.78e-02	0.054	1.00e+00	0.055
4	484	2.89e-03	0.072	5.58e-03	0.072	2.85e-02	0.072	9.93e-01	0.072
6	726	1.55e-03	0.107	1.54e-03	0.106	7.71e-04	0.107	1.51e-01	0.106
8	968	8.27e-04	0.143	4.23e-04	0.141	4.39e-04	0.142	4.94e-02	0.141
12	1452	3.84e-04	0.212	2.82e-05	0.210	1.11e-04	0.213	1.32e-02	0.212
16	1936	1.92e-04	0.283	9.63e-06	0.282	6.07e-05	0.283	7.17e-03	0.283
24	2904	1.07e-04	0.431	2.80e-06	0.427	2.80e-05	0.430	2.74e-03	0.424
32	3872	6.73e-05	0.579	1.90e-06	0.574	2.46e-05	0.579	2.61e-03	0.577
40	4840	3.58e-05	0.727	1.97e-06	0.728	2.28e-05	0.727	2.41e-03	0.729
48	5808	2.31e-05	0.886	1.93e-06	0.885	2.17e-05	0.888	2.27e-03	0.894
56	6776	1.40e-05	1.053	1.87e-06	1.055	2.01e-05	1.055	2.09e-03	1.059
64	7744	9.45e-06	1.224	1.57e-06	1.226	1.57e-05	1.225	1.60e-03	1.228
Coarse grid, 20×20									
1	441	3.14e-03	0.018	2.29e-01	0.019	1.00e+00	0.019	1.00e+00	0.018
2	882	3.64e-03	0.033	6.95e-02	0.034	8.84e-01	0.035	1.00e+00	0.034
3	1323	2.11e-03	0.049	3.37e-02	0.049	2.37e-02	0.050	9.96e-01	0.050
4	1764	8.88e-04	0.066	1.64e-03	0.067	2.65e-03	0.069	4.75e-01	0.065
6	2646	5.11e-04	0.097	1.19e-04	0.098	3.31e-04	0.100	2.74e-02	0.099
8	3528	1.84e-04	0.132	2.45e-05	0.133	4.98e-05	0.132	8.20e-03	0.131
12	5292	5.65e-05	0.204	3.66e-06	0.202	2.77e-05	0.203	3.60e-03	0.202
16	7056	3.15e-05	0.280	1.73e-06	0.279	1.33e-05	0.278	1.23e-03	0.278
24	10584	8.08e-06	0.450	9.29e-07	0.448	9.36e-06	0.447	6.50e-04	0.445
32	14112	5.38e-06	0.642	1.82e-06	0.640	4.70e-06	0.641	8.35e-04	0.638
40	17640	3.03e-06	0.862	1.79e-06	0.861	5.09e-06	0.855	8.41e-04	0.866
48	21168	1.87e-06	1.099	1.39e-06	1.098	3.70e-06	1.097	5.24e-04	1.110
56	24696	1.29e-06	1.378	1.26e-06	1.365	3.81e-06	1.372	3.03e-04	1.378
64	28224	8.91e-07	1.671	2.49e-07	1.673	1.05e-06	1.662	1.24e-04	1.646

Table 2: Test 2. Relative L_2 error (err) with time of solution (tm_s)

of multiscale basis functions. However, when comparing accuracy for a fixed number of coarse system DOFs, better results are typically achieved using the 10×10 grid with more multiscale basis functions. In Test 2, the coarse grid 10×10 and 20×20 results show a similar trend as in Test 1. We notice that for Tests 1 and 2 the proposed method gives a larger errors compared to Test 3. In Test 3, we achieve good results with a small number of basis functions J . Additionally, the impact of the coarse grid size is not as significant as in Tests 1 and 2. In all cases, we observe that we can achieve high levels of accuracy with a careful choice of coarse grid resolution and number of multiscale basis functions to balance the efficiency of computation and construction.

J	DOF_H	err 10^3	tm_s	err 10^6	tm_s	err 10^9	tm_s	err 10^{12}	tm_s
Coarse grid, 10×10									
1	121	2.26e-03	0.019	8.82e-03	0.020	8.78e-03	0.020	8.51e-03	0.020
2	242	5.22e-04	0.037	1.37e-03	0.037	9.00e-04	0.037	8.93e-04	0.037
3	363	4.08e-04	0.055	2.95e-03	0.055	6.60e-04	0.054	3.89e-04	0.056
4	484	2.35e-04	0.071	3.23e-04	0.072	2.17e-04	0.072	2.16e-04	0.071
6	726	1.34e-04	0.106	6.10e-05	0.106	5.99e-05	0.106	3.99e-04	0.106
8	968	8.54e-05	0.141	1.76e-05	0.141	6.01e-05	0.140	1.74e-04	0.141
12	1452	4.53e-05	0.213	4.55e-06	0.212	9.58e-06	0.212	1.44e-04	0.212
16	1936	2.33e-05	0.282	1.56e-06	0.285	2.14e-06	0.284	3.66e-05	0.284
24	2904	9.60e-06	0.431	6.75e-07	0.430	8.35e-07	0.429	6.00e-06	0.430
32	3872	3.77e-06	0.579	4.12e-07	0.581	4.19e-07	0.579	1.35e-06	0.582
40	4840	1.96e-06	0.734	3.32e-07	0.732	3.73e-07	0.733	2.34e-06	0.726
48	5808	1.44e-06	0.894	3.10e-07	0.893	3.11e-07	0.886	4.14e-07	0.892
56	6776	9.65e-07	1.058	2.97e-07	1.050	2.97e-07	1.054	3.95e-07	1.050
64	7744	7.56e-07	1.219	2.89e-07	1.235	2.89e-07	1.225	3.02e-07	1.231
Coarse grid, 20×20									
1	441	5.74e-04	0.018	5.23e-03	0.018	5.18e-03	0.018	4.88e-03	0.018
2	882	2.04e-04	0.033	5.58e-04	0.034	4.86e-04	0.034	2.24e-04	0.034
3	1323	1.82e-04	0.050	1.48e-03	0.049	3.14e-04	0.049	7.41e-05	0.049
4	1764	5.48e-05	0.067	3.86e-05	0.066	2.03e-04	0.066	1.55e-04	0.066
6	2646	3.36e-05	0.099	4.81e-06	0.098	3.87e-05	0.098	2.11e-04	0.100
8	3528	1.64e-05	0.131	1.43e-06	0.131	3.46e-06	0.132	1.14e-04	0.132
12	5292	4.46e-06	0.203	4.90e-07	0.204	1.14e-06	0.206	2.06e-05	0.206
16	7056	1.89e-06	0.281	3.23e-07	0.282	4.13e-07	0.280	4.33e-06	0.281
24	10584	6.26e-07	0.449	2.42e-07	0.452	2.95e-07	0.446	1.56e-06	0.447
32	14112	3.63e-07	0.644	2.31e-07	0.655	2.83e-07	0.651	2.17e-06	0.644
40	17640	2.25e-07	0.870	2.13e-07	0.861	2.31e-07	0.864	5.63e-07	0.858
48	21168	1.77e-07	1.111	2.06e-07	1.108	2.44e-07	1.100	2.95e-07	1.094
56	24696	1.56e-07	1.369	1.96e-07	1.379	2.57e-07	1.398	4.37e-07	1.368
64	28224	1.44e-07	1.658	1.82e-07	1.713	5.02e-07	1.703	1.87e-06	1.646

Table 3: Test 3. Relative L_2 error (err) with time of solution (tm_s)

5.2. Two-grid multiscale preconditioner

In this section, we consider the performance of the proposed multiscale solver as a two-grid preconditioner for the conjugate gradient iterative solver from Scipy sparse library [49]. As a smoother, we use five Jacobi and Gauss-Seidel iterations ($\nu = 5$) from pyamg library [4, 5]. To stop iterations, we use a default set of parameters in PCG with relative tolerance $r_{tol} = 10^{-5}$ and set 100 as the maximum number of iterations (nc indicates no convergence within the given restrictions).

We consider the same test problems on a fine grid with $DOF_h = 201,385$. We simulate with $t_{max} = 5 \cdot 10^{-6}$ using $N_t = 10$ time steps. For a coarse grid solver, we use the 10×10 and 20×20 multiscale approximation described in the previous section. We compare the performance of the pro-

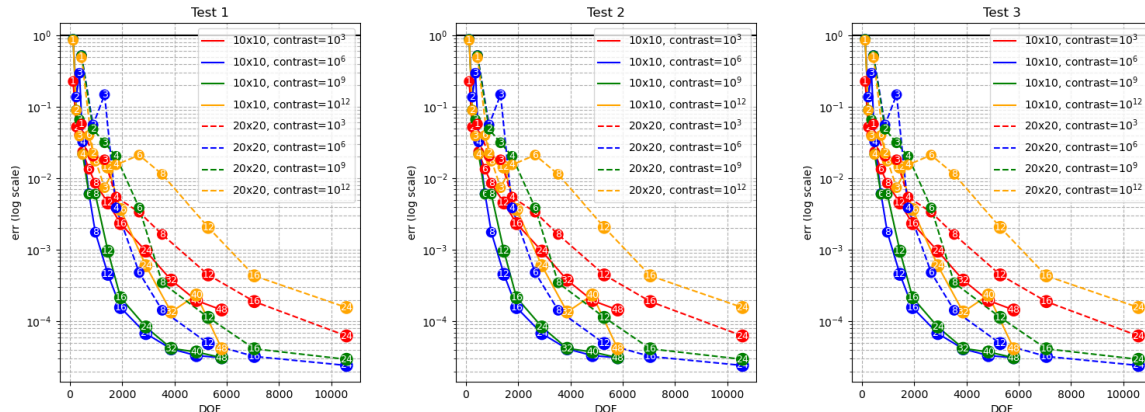


Figure 4: Error vs DOF_H for Tests 1, 2 and 3 (from left to right).

posed preconditioner with several classic multilevel AMG solvers from the PyAMG library. We consider three AMG preconditioners with pre- and post-smoothing to match the spectral two-level method, and default parameters from the PyAMG library (which have generally been tuned for robust performance): (1) mg_1 is a classical smoothed aggregation multilevel solver; (2) mg_2 is a classical AMG (Ruge-Stuben AMG) solver without second-pass coarsening; and (3) mg_3 is the same solver as mg_2 with second-pass coarsening for the C/F splitting (typically resulting in slower coarsening, but improved convergence). We investigate an average number of iterations for PCG per time iteration, $\bar{N} = \bar{N}_{tot}/N_t$, where \bar{N}_{tot} is the total number of iterations. The results are presented with the time required for online computations (tm_s) for varying numbers of multiscale basis functions that directly affect the accuracy of the coarse grid approximation and size of the coarse grid system.

First and foremost, Tables 4, 5, and 6 demonstrate that the two-grid preconditioning built on a GMSFEM spectral coarse space is robust with respect to anisotropy. For all test cases, with sufficient coarse grid basis functions on a 20×20 coarse grid, excellent convergence rates can be obtained that are independent of anisotropy. On a 10×10 coarse grid, there is modest growth in iteration count from 10^3 to 10^6 anisotropy ratio, even for a large number of basis functions, but robust convergence is still obtained at anisotropy ratio 10^6 , which does not increase as the anisotropy ratio further increases. In general, the 10×10 coarse grid typically requires $2 - 3 \times$ as many basis functions as the 20×20 coarse grid (usually closer to two) for comparable convergence. But, if basis functions can be computed offline, this would still be more efficient in practice, as the coarse grid operator is still smaller. We also point out that iteration counts monotonically decreases with increased coarse basis functions in almost all cases; in particular, indicating that convergence does not stall with respect to local basis functions, and can seemingly always be improved with more, down to $\mathcal{O}(1)$ iterations in many cases. The solve time also generally decreases with increased basis functions, at some point stagnating but rarely increasing notably. Again, if basis functions can be computed offline, this indicates that generally choosing more local basis functions will make for a rapidly converging and robust method.

Finally, we point out that Test 3 (see Table 6), which appears to have the most complex field lines, generally observes the best and most robust convergence, particularly for large anisotropies. Test 3 also benefits significantly from symmetric Gauss-Seidel relaxation compared with Jacobi. Although iteration

J	N 10^3 tm_s		N 10^6 tm_s		N 10^9 tm_s		N 10^{12} tm_s		N 10^3 tm_s		N 10^6 tm_s		N 10^9 tm_s		N 10^{12} tm_s	
	Jacobi smoother								Gauss-Seidel smoother							
	Coarse grid, 10×10															
1	25	10.2	nc	-	nc	-	nc	-	15	8.7	nc	-	nc	-	nc	-
2	24	9.8	nc	-	nc	-	nc	-	15	8.6	nc	-	nc	-	nc	-
3	24	9.9	nc	-	nc	-	nc	-	15	8.8	nc	-	nc	-	nc	-
4	24	9.6	nc	-	nc	-	nc	-	15	8.3	nc	-	nc	-	nc	-
6	23	9.8	nc	-	nc	-	nc	-	15	8.2	nc	-	nc	-	nc	-
8	23	8.2	nc	-	nc	-	nc	-	15	7.7	nc	-	nc	-	nc	-
12	23	9.8	nc	-	nc	-	nc	-	15	8.7	nc	-	nc	-	nc	-
16	23	11.5	84	42.3	nc	-	nc	-	15	9.8	62	40.6	nc	-	nc	-
24	22	14.2	53	34.3	91	59.0	94	61.6	14	11.2	38	30.4	54	43.3	57	45.8
32	21	16.7	36	28.7	50	39.8	52	41.5	13	12.3	25	23.7	30	28.5	31	29.4
40	20	19.0	33	31.3	40	38.0	41	39.0	13	14.3	22	24.3	24	26.6	25	27.7
48	19	21.1	30	33.3	34	37.8	35	39.0	13	16.4	20	25.3	21	26.7	21	26.6
56	18	23.0	26	33.2	29	36.9	30	38.3	12	17.2	18	25.7	19	27.0	19	27.1
64	17	24.5	22	31.9	25	36.2	26	37.6	11	17.6	15	23.9	16	25.7	16	25.6
	Coarse grid, 20×20															
1	24	6.8	nc	-	nc	-	nc	-	15	6.4	nc	-	nc	-	nc	-
2	24	6.6	nc	-	nc	-	nc	-	15	6.2	nc	-	nc	-	nc	-
3	23	6.7	nc	-	nc	-	nc	-	15	6.3	nc	-	nc	-	nc	-
4	23	6.2	nc	-	nc	-	nc	-	15	6.2	nc	-	nc	-	nc	-
6	23	7.1	nc	-	nc	-	nc	-	15	6.8	99	44.6	nc	-	nc	-
8	22	7.5	86	28.9	nc	-	nc	-	15	7.4	62	30.0	nc	-	nc	-
12	21	8.6	50	20.1	86	35.1	89	36.3	14	7.9	35	19.3	53	29.4	55	30.2
16	19	9.2	34	16.2	49	23.7	51	24.6	13	8.3	23	14.4	29	18.4	31	19.3
24	15	9.6	19	12.1	24	15.5	25	16.1	10	8.0	13	10.2	15	12.0	15	11.8
32	14	11.6	16	13.2	18	14.8	18	15.0	9	9.0	11	10.7	11	10.9	11	10.7
40	12	12.6	13	13.5	14	14.8	14	14.6	8	9.6	9	10.6	9	10.8	9	10.7
48	11	14.1	12	15.3	12	15.3	12	15.2	7	9.9	8	11.2	8	11.3	7	9.9
56	10	15.4	11	16.6	11	16.8	11	16.7	7	11.9	7	11.7	7	12.0	7	11.6
64	9	16.3	10	17.9	10	18.2	9	16.3	6	11.9	7	13.8	6	11.9	6	11.8
mg ₁	36	9.3	nc	-	nc	-	nc	-	16	4.2	nc	-	nc	-	nc	-
mg ₂	34	14.5	nc	-	nc	-	nc	-	21	9.1	nc	-	nc	-	nc	-
mg ₃	27	18.0	nc	-	nc	-	nc	-	18	12.0	nc	-	nc	-	nc	-

Table 4: Test 1. Average number of iterations \bar{N} with time of solution tm_s

counts are fairly large, with Gauss Seidel we are able to converge for only 1 coarse basis function on the 10×10 grid. We believe this is due to a large percentage of acyclic/open field lines in test 3, as opposed to the exclusively closed field lines in Tests 1 and 2. Closed field lines make the linear system particularly more ill-conditioned and challenging to solve, as in one time step heat will traverse the domain many times. In contrast, with open field lines there is a particular benefit to a Gauss-Seidel relaxation, which can relax on a given field line across the whole domain, boundary to boundary, analogous to an

J	N 10^3	tm_s	N 10^6	tm_s	N 10^9	tm_s	N 10^{12}	tm_s	N 10^3	tm_s	N 10^6	tm_s	N 10^9	tm_s	N 10^{12}	tm_s
	Jacobi smoother								Gauss-Seidel smoother							
	Coarse grid, 10×10															
1	26	7.5	nc	-	nc	-	nc	-	15	8.1	nc	-	nc	-	nc	-
2	25	7.5	nc	-	nc	-	nc	-	15	8.1	nc	-	nc	-	nc	-
3	24	7.4	nc	-	nc	-	nc	-	15	8.0	nc	-	nc	-	nc	-
4	24	7.7	nc	-	nc	-	nc	-	15	7.9	nc	-	nc	-	nc	-
6	23	7.8	nc	-	nc	-	nc	-	15	8.1	nc	-	nc	-	nc	-
8	23	8.5	nc	-	nc	-	nc	-	15	7.7	nc	-	nc	-	nc	-
12	23	9.9	nc	-	nc	-	nc	-	15	8.7	93	54.8	nc	-	nc	-
16	23	11.4	83	41.4	nc	-	nc	-	15	9.8	57	37.5	65	42.9	64	42.4
24	22	14.2	52	33.5	48	31.0	48	31.0	14	11.2	38	30.4	29	23.3	28	22.9
32	21	16.7	37	29.4	30	23.8	29	23.1	13	12.3	25	23.7	18	17.1	18	17.1
40	20	18.9	32	30.4	24	45.1	23	22.6	13	14.4	22	24.2	15	16.5	14	15.6
48	19	21.0	28	31.0	20	22.1	20	22.3	12	15.1	19	24.0	12	15.1	12	15.2
56	18	22.9	26	33.2	18	53.1	17	21.6	12	17.1	17	24.2	11	15.7	11	15.7
64	17	24.5	23	33.3	16	23.1	16	23.1	11	17.6	16	25.7	10	16.0	10	16.0
	Coarse grid, 20×20															
1	24	6.7	nc	-	nc	-	nc	-	16	6.7	nc	-	nc	-	nc	-
2	24	6.8	nc	-	nc	-	nc	-	16	6.8	nc	-	nc	-	nc	-
3	23	6.3	nc	-	nc	-	nc	-	15	6.8	nc	-	nc	-	nc	-
4	23	6.2	nc	-	nc	-	nc	-	15	6.3	nc	-	nc	-	nc	-
6	23	6.9	nc	-	nc	-	nc	-	15	6.8	86	39.0	98	44.9	98	44.1
8	22	7.4	84	28.3	nc	-	nc	-	15	7.3	54	26.3	63	30.7	62	30.1
12	21	8.6	49	19.9	45	18.5	45	18.0	14	7.8	34	19.0	27	15.1	27	14.8
16	19	9.1	33	15.9	28	13.4	27	13.2	13	8.2	22	13.9	17	10.7	16	10.4
24	16	10.2	21	13.5	14	8.9	14	8.9	11	8.7	14	11.1	9	7.1	9	7.1
32	14	11.6	16	13.2	11	9.1	11	9.0	9	8.9	11	10.7	7	6.8	7	6.8
40	12	12.6	13	13.4	9	9.4	9	9.3	8	9.5	9	10.7	6	7.2	6	7.1
48	11	14.1	12	15.3	8	10.3	8	10.1	7	9.9	8	11.4	5	7.2	5	7.0
56	10	15.3	11	16.9	7	10.8	7	10.6	7	11.8	7	11.7	5	8.5	4	6.7
64	9	16.3	10	17.9	6	10.9	6	10.7	6	11.8	7	13.6	4	8.0	4	8.0
mg ₁	36	9.3	nc	-	nc	-	nc	-	17	4.4	nc	-	nc	-	nc	-
mg ₂	31	13.3	nc	-	nc	-	nc	-	19	8.2	nc	-	nc	-	nc	-
mg ₃	24	16.0	nc	-	nc	-	nc	-	16	10.6	nc	-	nc	-	nc	-

Table 5: Test 2. Average number of iterations \bar{N} with time of solution tm_s

approximate line relaxation.

6. Conclusion

Here we present a multiscale finite element method to solve the heat flux problem with strong anisotropy. The presented method is based on constructing spectral multiscale basis functions and

J	N 10^3	tm_s	N 10^6	tm_s	N 10^9	tm_s	N 10^{12}	tm_s	N 10^3	tm_s	N 10^6	tm_s	N 10^9	tm_s	N 10^{12}	tm_s
	Jacobi smoother							Gauss-Seidel smoother								
	Coarse grid, 10×10															
1	19	7.2	nc	-	nc	-	nc	-	12	8.1	91	61.7	97	65.4	97	65.8
2	19	7.5	nc	-	nc	-	nc	-	12	8.3	83	57.9	83	57.9	83	57.8
3	19	7.8	nc	-	nc	-	nc	-	12	8.5	73	52.5	73	51.7	73	51.9
4	19	8.2	nc	-	nc	-	nc	-	11	8.0	66	48.7	67	48.7	67	48.8
6	18	8.2	nc	-	nc	-	nc	-	11	8.4	55	42.1	57	43.3	57	44.0
8	26	9.3	nc	-	nc	-	nc	-	15	7.7	67	34.1	64	32.6	67	34.5
12	25	10.7	96	41.5	99	42.3	99	42.5	15	8.7	48	27.9	49	28.5	49	28.7
16	24	12.0	86	42.9	89	44.4	89	44.7	14	9.2	46	30.0	46	30.0	46	30.1
24	23	14.9	62	40.0	62	40.1	62	40.2	13	10.4	32	25.5	32	25.5	32	25.6
32	22	17.6	44	35.0	44	35.0	44	35.1	13	12.4	24	22.7	24	22.7	24	22.9
40	21	20.0	40	37.9	40	37.9	40	38.0	12	13.3	21	23.1	21	23.1	21	23.2
48	20	22.2	35	38.8	35	38.8	35	39.0	12	15.2	19	24.0	19	24.0	19	24.0
56	19	24.3	31	39.5	32	40.7	32	40.8	11	15.7	17	24.3	17	24.3	17	24.3
64	18	26.2	28	40.5	28	40.4	28	40.6	10	16.0	15	24.0	15	24.1	15	24.0
	Coarse grid, 20×20															
1	26	5.6	nc	-	nc	-	nc	-	16	5.9	nc	-	nc	-	nc	-
2	27	6.3	nc	-	nc	-	nc	-	16	6.2	nc	-	nc	-	nc	-
3	26	6.4	nc	-	nc	-	nc	-	15	6.0	81	32.9	81	32.9	80	32.5
4	26	6.9	nc	-	nc	-	nc	-	15	6.2	63	26.6	68	29.1	68	28.5
6	24	7.1	94	28.4	94	28.7	94	29.2	14	6.3	43	19.7	43	19.7	43	19.7
8	23	7.6	75	25.1	77	26.1	77	26.4	13	6.2	36	17.5	36	17.7	36	17.5
12	20	7.9	47	18.9	47	19.0	47	19.2	12	6.5	25	14.0	25	14.0	25	14.0
16	19	8.9	34	16.2	34	16.4	34	16.3	11	6.8	17	10.7	17	10.8	17	10.8
24	16	10.1	21	13.5	21	13.4	21	13.5	10	7.8	12	9.6	12	9.5	12	9.5
32	14	11.5	18	15.0	18	14.9	18	15.1	8	318.7	10	9.9	10	9.8	10	9.8
40	12	12.4	14	14.7	14	14.5	14	14.7	7	8.1	8	9.5	8	9.5	8	9.5
48	11	13.8	12	15.2	12	15.2	12	15.4	7	9.7	7	10.0	7	10.0	7	10.0
56	10	15.2	11	16.9	11	16.8	11	16.8	6	9.9	6	9.9	6	10.2	6	10.1
64	9	16.9	9	16.8	9	16.3	9	16.4	6	11.6	6	11.8	6	11.7	6	11.7
mg ₁	31	8.1	nc	-	nc	-	nc	-	10	2.6	31	8.0	33	8.7	33	8.6
mg ₂	30	12.8	nc	-	nc	-	nc	-	17	7.3	nc	-	nc	-	nc	-
mg ₃	24	15.8	nc	-	nc	-	nc	-	14	9.3	nc	-	nc	-	nc	-

Table 6: Test 3. Average number of iterations \bar{N} with time of solution tm_s

Galerkin coupling on the coarse grid. We have demonstrated that the presented basis functions are aligned with magnetic fields and produce excellent approximation for problems with high contrast between parallel and perpendicular flow directions. We demonstrate the potential of the multiscale basis functions in two contexts, (i) as a surrogate model with significantly reduced size, and (ii) as the coarse-grid correction in a two-level preconditioner. The latter is particularly relevant for extreme anisotropies as considered in this paper, because efficient implicit solvers remain a largely open question. The signifi-

cantly reduced system size provided by the multiscale basis functions makes direct or sparse approximate inverses computationally tractable on the coarse grid, and we utilize only standard pointwise Jacobi or Gauss-Seidel relaxation on the fine grid.

Numerical results demonstrate the method's convergence with respect to the number of spectral basis functions and coarse grid resolution. We have presented results for three test cases with different magnetic field distributions and varying anisotropy ratios. The results show how a careful choice of the basis functions, with respect to the given magnetic field, can produce very good results for problems with very high anisotropy. Future work will consider more challenging and realistic test cases, applying the multiscale methodology to more specialized discretizations, e.g. [50, 51], and developing efficient computational approaches for magnetic fields that evolve nonlinearly with the physical variables.

Acknowledgements

BSS and GW work was supported by the Laboratory Directed Research and Development program of Los Alamos National Laboratory under project number 20240261ER. LA-UR-24-32768.

Appendix A. Multiscale space

We define $w^n \in V_H$ as the elliptic projection of $T_h^n \in V_h$ ($w^n = \Pi T_h^n$) that satisfies (16) and

$$a(T_h^n - w^n, v) = 0, \quad \forall v \in V_H.$$

For any $v \in V_H$, we have the following error equation

$$m(T_h^n - T_{ms}^n, v) - m(T_h^{n-1} - T_{ms}^{n-1}, v) + \tau a(T_h^n - T_{ms}^n, v) = m(T_h^n - T_h^{n-1}, v) + \tau a(T_h^n, v) - \tau(f, v) = 0.$$

We set $v = w^n - T_{ms}^n = (T_h^n - T_{ms}^n) - (T_h^n - w^n)$ and obtain

$$\begin{aligned} & \underbrace{m(T_h^n - T_{ms}^n, T_h^n - T_{ms}^n)}_{I_1} + \tau \underbrace{a(T_h^n - T_{ms}^n, T_h^n - T_{ms}^n)}_{I_2} \\ &= \underbrace{m(T_h^n - T_{ms}^n, T_h^n - w^n)}_{I_3} + \underbrace{m(T_h^{n-1} - T_{ms}^{n-1}, w^n - T_{ms}^n)}_{I_4} + \tau \underbrace{a(T_h^n - T_{ms}^n, T_h^n - w^n)}_{I_5}. \end{aligned}$$

For the first and second terms, we have

$$I_1 : \quad m(T_h^n - T_{ms}^n, T_h^n - T_{ms}^n) = \|T_h^n - T_{ms}^n\|_{M_h}^2,$$

$$I_2 : \quad a(T_h^n - T_{ms}^n, T_h^n - T_{ms}^n) = \|T_h^n - T_{ms}^n\|_{A_h}^2.$$

For the third and fifth terms by Cauchy-Schwarz and Young's inequalities, we obtain

$$I_3 : \quad m(T_h^n - T_{ms}^n, T_h^n - w^n) \leq \frac{1}{4\delta_1} \|T_h^n - T_{ms}^n\|_{M_h}^2 + \delta_1 \|T_h^n - w^n\|_{M_h}^2,$$

$$I_5 : \quad a(T_h^n - T_{ms}^n, T_h^n - w^n) \leq \frac{1}{4\delta_2} \|T_h^n - T_{ms}^n\|_{A_h}^2 + \delta_2 \|T_h^n - w^n\|_{A_h}^2.$$

For the fourth term with $w^n - T_{ms}^n = (w^n - T_h^n) + (T_h^n - T_{ms}^n)$, we have

$$\begin{aligned}
I_4 &: m(T_h^{n-1} - T_{ms}^{n-1}, w^n - T_{ms}^n) \\
&= m(T_h^{n-1} - T_{ms}^{n-1}, w^n - T_h^n) + m(T_h^{n-1} - T_{ms}^{n-1}, T_h^n - T_{ms}^n) \\
&\leq \frac{1}{2\delta_3} \|T_h^{n-1} - T_{ms}^{n-1}\|_{M_h}^2 + \delta_3 \|w^n - T_h^n\|_{M_h}^2 + \delta_3 \|T_h^n - T_{ms}^n\|_{M_h}^2.
\end{aligned}$$

Then, we have

$$\begin{aligned}
&\|T_h^n - T_{ms}^n\|_{M_h}^2 + \tau \|T_h^n - T_{ms}^n\|_{A_h}^2 \\
&\leq \frac{1}{2\delta_3} \|T_h^{n-1} - T_{ms}^{n-1}\|_{M_h}^2 + \delta_3 \|w^n - T_h^n\|_{M_h}^2 + \delta_3 \|T_h^n - T_{ms}^n\|_{M_h}^2 \\
&\quad + \frac{1}{4\delta_1} \|T_h^n - T_{ms}^n\|_{M_h}^2 + \delta_1 \|T_h^n - w^n\|_{M_h}^2 + \frac{\tau}{4\delta_2} \|T_h^n - T_{ms}^n\|_{A_h}^2 + \tau\delta_2 \|T_h^n - w^n\|_{A_h}^2 \\
&= \frac{1}{2\delta_3} \|T_h^{n-1} - T_{ms}^{n-1}\|_{M_h}^2 + (\delta_3 + \delta_1) \|T_h^n - w^n\|_{M_h}^2 + \left(\delta_3 + \frac{1}{4\delta_1}\right) \|T_h^n - T_{ms}^n\|_{M_h}^2 \\
&\quad + \frac{\tau}{4\delta_2} \|T_h^n - T_{ms}^n\|_{A_h}^2 + \tau\delta_2 \|T_h^n - w^n\|_{A_h}^2.
\end{aligned}$$

We can rewrite the estimate as follows

$$\begin{aligned}
&\left(1 - \delta_3 - \frac{1}{4\delta_1}\right) \|T_h^n - T_{ms}^n\|_{M_h}^2 + \tau \left(1 - \frac{1}{4\delta_2}\right) \|T_h^n - T_{ms}^n\|_{A_h}^2 \\
&\leq \frac{1}{2\delta_3} \|T_h^{n-1} - T_{ms}^{n-1}\|_{M_h}^2 + (\delta_3 + \delta_1) \|T_h^n - w^n\|_{M_h}^2 + \tau\delta_2 \|T_h^n - w^n\|_{A_h}^2.
\end{aligned}$$

For $\delta_1 = 1$, $\delta_2 = 1/2$ and $\delta_3 = 1/4$, we obtain

$$\|T_h^n - T_{ms}^n\|_{M_h}^2 + \tau \|T_h^n - T_{ms}^n\|_{A_h}^2 \leq \|T_h^{n-1} - T_{ms}^{n-1}\|_{M_h}^2 + \|T_h^n - w^n\|_{M_h}^2 + \tau \|T_h^n - w^n\|_{A_h}^2.$$

Therefore

$$\|T_h^n - T_{ms}^n\|_{M_h}^2 + \tau \sum_{k=1}^n \|T_h^k - T_{ms}^k\|_{A_h}^2 \leq \|T_h^0 - T_{ms}^0\|_{M_h}^2 + \sum_{k=1}^n (\|T_h^k - w^k\|_{M_h}^2 + \tau \|T_h^k - w^k\|_{A_h}^2).$$

Then, using estimates (16)

$$\begin{aligned}
\|T_h^k - w^k\|_{A_h}^2 &\leq \left(\frac{1}{H^2\lambda_{J+1}^2} + \frac{1}{\lambda_{J+1}}\right) \|B_h T_h^k\|_{D_h}^2, \\
\|T_h^k - w^k\|_{M_h}^2 &\leq \|T_h^k - w^k\|_{D_h}^2 \leq \frac{1}{\lambda_{J+1}^2} \|B_h T_h^k\|_{D_h}^2,
\end{aligned}$$

we obtain the result

$$\begin{aligned}
&\|T_h^n - T_{ms}^n\|_{M_h}^2 + \tau \sum_{k=1}^n \|T_h^k - T_{ms}^k\|_{A_h}^2 \\
&\leq \|T_h^0 - T_{ms}^0\|_{M_h}^2 + \sum_{k=1}^n \left(\frac{1}{\lambda_{J+1}^2} + \tau \left(\frac{1}{H^2\lambda_{J+1}^2} + \frac{1}{\lambda_{J+1}}\right)\right) \|B_h T_h^k\|_{D_h}^2 \\
&\leq \|T_h^0 - T_{ms}^0\|_{M_h}^2 + \tau \sum_{k=1}^n \frac{1}{\lambda_{J+1}} \|B_h T_h^k\|_{D_h}^2.
\end{aligned}$$

By scaling eigenvalues with H^{-2} ($\lambda_{J+1} = H^{-2}\Lambda^*$) for moving to size one domain [1]

$$\|T_h^n - T_{ms}^n\|_{M_h}^2 + \tau \sum_{k=1}^n \|T_h^n - T_{ms}^n\|_{A_h}^2 \preceq \|T_h^0 - T_{ms}^0\|_{M_h}^2 + \tau \sum_{k=1}^n \frac{H^2}{\Lambda^*} \|B_h T_h^k\|_{D_h}^2$$

Finally, under some additional regularity and appropriate initial conditions, we have an error of order $\mathcal{O}(\tau \frac{H^2}{\Lambda^*})$, where Λ^* is responsible for covering a highly anisotropic flow by a spectral coarse space.

Appendix B. Two-grid convergence

Let $\|v\|_{Q_h}$ be a τ -weighted H_1 norm [3]

$$\|v\|_{Q_h}^2 = v^T Q_h v = v^T \left(\frac{1}{\tau} M_h + A_h \right) v = \frac{1}{\tau} \|v\|_{M_h}^2 + \|v\|_{A_h}^2.$$

The two-grid error propagation can be expressed as follows [20, 47]

$$E_{TG} = I - C_{TG}^{-1} Q_h$$

with

$$C_{TG}^{-1} = \bar{S}^{-1} + (I - S^{-T} Q_h) P Q_H^{-1} P^T (I - Q_h S^{-1}), \quad \bar{S} = S(S + S^T - Q_h)^{-1} S^T.$$

We have

$$\|v\|_{Q_h}^2 \leq v^T C_{TG} v \leq K_{TG} \|v\|_{Q_h}^2, \quad \text{where } K_{TG} := \text{Cond}(C_{TG}^{-1} Q_h),$$

and

$$0 \leq v^T Q_h E_{TG} v \leq \left(1 - \frac{1}{K_{TG}} \right) \|v\|_{Q_h}^2.$$

For typical smoothers (Jacobi, Gauss-Seidel), we have $Q_h = D_Q - N_Q - N_Q^T$, where D_Q is the diagonal of Q_h and $-N_Q$ is the strictly lower triangular part of Q_h . Then $S = D_Q - N_Q$ for Gauss-Seidel smoother and $S = D_Q$ for Jacobi and \tilde{S} is the symmetric matrix that is spectrally equivalent to D_Q [47]. Moreover, we have spectral equivalency of smoother S to $D_Q = \text{diag}(Q_h)$.

Based on the theory of two-grid method in [47, 8, 20, 52], we have

$$K_{TG} = \sup_v \frac{\|v - \Pi v\|_{D_Q}^2}{\|v\|_{Q_h}^2}.$$

Using estimate (16), we obtain

$$\|v - \Pi v\|_{D_Q}^2 \leq \left(1 + \frac{C}{\tau} \right) \|v - \Pi v\|_{D_h}^2 \leq \left(1 + \frac{C}{\tau} \right) \frac{H^2}{\Lambda^*} \|v\|_{A_h}^2 \leq \left(1 + \frac{C}{\tau} \right) \frac{H^2}{\Lambda^*} \|v\|_{Q_h}^2$$

and we have $K_{TG} = \left(1 + \frac{C}{\tau} \right) \frac{H^2}{\Lambda^*}$.

References

- [1] Eduardo Abreu, Ciro Díaz, and Juan Galvis. A convergence analysis of generalized multiscale finite element methods. *Journal of Computational Physics*, 396:303–324, 2019.
- [2] I Yucel Akkutlu, Yalchin Efendiev, Maria Vasilyeva, and Yuhe Wang. Multiscale model reduction for shale gas transport in poroelastic fractured media. *Journal of Computational Physics*, 353:356–376, 2018.
- [3] IY Akkutlu, Yalchin Efendiev, and Maria Vasilyeva. Multiscale model reduction for shale gas transport in fractured media. *Computational Geosciences*, pages 1–21, 2015.
- [4] Nathan Bell, Luke N Olson, and Jacob Schroder. Pyamg: Algebraic multigrid solvers in python. *Journal of Open Source Software*, 7(72):4142, 2022.
- [5] Nathan Bell, Luke N Olson, Jacob Schroder, and Ben Southworth. Pyamg: algebraic multigrid solvers in python. *Journal of Open Source Software*, 8(87):5495, 2023.
- [6] Stefano Berrone, Stefano Scialò, and Gioana Teora. The mixed virtual element discretization for highly-anisotropic problems: the role of the boundary degrees of freedom. *arXiv preprint arXiv:2307.16474*, 2023.
- [7] A. Brandt, J. Brannick, K. Kahl, and I. Livshits. Algebraic distance for anisotropic diffusion problems: multilevel results, 2014. arXiv:1409.4702.
- [8] Marian Brezina and Panayot S Vassilevski. Smoothed aggregation spectral element agglomeration amg: Sa- ρ amge. In *International Conference on Large-Scale Scientific Computing*, pages 3–15. Springer, 2011.
- [9] William L. Briggs, Van Emden Henson, and Steve F. McCormick. *A Multigrid Tutorial, Second Edition*. Society for Industrial and Applied Mathematics, second edition, 2000.
- [10] Amareshwara Sainadh Chamarthi, Hiroaki Nishikawa, and Kimiya Komurasaki. First order hyperbolic approach for anisotropic diffusion equation. *Journal of Computational Physics*, 396:243–263, 2019.
- [11] Tim Chartier, Robert D Falgout, VE Henson, J Jones, T Manteuffel, S McCormick, J Ruge, and Panayot S Vassilevski. Spectral amge (ρ amge). *SIAM Journal on Scientific Computing*, 25(1):1–26, 2003.
- [12] Timothy Chartier, Robert Falgout, Van Emden Henson, Jim E Jones, Tom A Manteuffel, John W Ruge, Steve F McCormick, and Panayot S Vassilevski. Spectral element agglomerate amge. In *Domain decomposition methods in science and engineering XVI*, pages 513–521. Springer, 2007.
- [13] Eric T Chung, Yalchin Efendiev, and Wing Tat Leung. Constraint energy minimizing generalized multiscale finite element method. *Computer Methods in Applied Mechanics and Engineering*, 339:298–319, 2018.
- [14] Eric T Chung, Yalchin Efendiev, Wing Tat Leung, Maria Vasilyeva, and Yating Wang. Non-local multi-continua upscaling for flows in heterogeneous fractured media. *Journal of Computational Physics*, 372:22–34, 2018.

- [15] Eric T Chung, Yalchin Efendiev, Guanglian Li, and Maria Vasilyeva. Generalized multiscale finite element methods for problems in perforated heterogeneous domains. *Applicable Analysis*, 95(10):2254–2279, 2016.
- [16] Eric T Chung, Wing Tat Leung, Maria Vasilyeva, and Yating Wang. Multiscale model reduction for transport and flow problems in perforated domains. *Journal of Computational and Applied Mathematics*, 330:519–535, 2018.
- [17] Yalchin Efendiev, Juan Galvis, and Thomas Y Hou. Generalized multiscale finite element methods (gmsfem). *Journal of computational physics*, 251:116–135, 2013.
- [18] Yalchin Efendiev, Juan Galvis, and Panayot S Vassilevski. Multiscale spectral amge solvers for high-contrast flow problems. *ISC-Preprint, Texas A&M University*, 2012.
- [19] Yalchin Efendiev, Juan Galvis, and Xiao-Hui Wu. Multiscale finite element methods for high-contrast problems using local spectral basis functions. *Journal of Computational Physics*, 230(4):937–955, 2011.
- [20] Robert D Falgout, Panayot S Vassilevski, and Ludmil T Zikatanov. On two-grid convergence estimates. *Numerical linear algebra with applications*, 12(5-6):471–494, 2005.
- [21] Juan Galvis and Yalchin Efendiev. Domain decomposition preconditioners for multiscale flows in high-contrast media. *Multiscale Modeling & Simulation*, 8(4):1461–1483, 2010.
- [22] Michael W Gee, Jonathan J Hu, and Raymond S Tuminaro. A new smoothed aggregation multigrid method for anisotropic problems. *Numerical Linear Algebra with Applications*, 16(1):19–37, 2009.
- [23] Christophe Geuzaine and Jean-François Remacle. Gmsh: A 3-d finite element mesh generator with built-in pre-and post-processing facilities. *International journal for numerical methods in engineering*, 79(11):1309–1331, 2009.
- [24] Giorgio Giorgiani, Hugo Bufferand, Frédéric Schwander, Eric Serre, and P Tamain. A high-order non field-aligned approach for the discretization of strongly anisotropic diffusion operators in magnetic fusion. *Computer Physics Communications*, 254:107375, 2020.
- [25] David Green, Xiaozhe Hu, Jeremy Lore, Lin Mu, and Mark L Stowell. An efficient high-order numerical solver for diffusion equations with strong anisotropy. *Computer Physics Communications*, 276:108333, 2022.
- [26] Sibylle Günter, Karl Lackner, and C Tichmann. Finite element and higher order difference formulations for modelling heat transport in magnetised plasmas. *Journal of Computational Physics*, 226(2):2306–2316, 2007.
- [27] Dmitri Kuzmin, Mikhail J Shashkov, and Daniil Svyatskiy. A constrained finite element method satisfying the discrete maximum principle for anisotropic diffusion problems. *Journal of Computational Physics*, 228(9):3448–3463, 2009.
- [28] Anders Logg, Kent-Andre Mardal, and Garth Wells. *Automated solution of differential equations by the finite element method: The FEniCS book*, volume 84. Springer Science & Business Media, 2012.

- [29] Thomas A Manteuffel, Steffen Münzenmaier, John Ruge, and Ben Southworth. Nonsymmetric reduction-based algebraic multigrid. *SIAM Journal on Scientific Computing*, 41(5):S242–S268, 2019.
- [30] Thomas A Manteuffel, Luke N Olson, Jacob B Schroder, and Ben S Southworth. A root-node-based algebraic multigrid method. *SIAM Journal on Scientific Computing*, 39(5):S723–S756, 2017.
- [31] Thomas A Manteuffel, John Ruge, and Ben S Southworth. Nonsymmetric algebraic multigrid based on local approximate ideal restriction (IAIR). *SIAM Journal on Scientific Computing*, 40(6):A4105–A4130, 2018.
- [32] Tom Manteuffel and Ben S Southworth. Convergence in norm of nonsymmetric algebraic multigrid. *SIAM Journal on Scientific Computing*, 41(5):S269–S296, 2019.
- [33] Jens M Melenk and Ivo Babuška. The partition of unity finite element method: basic theory and applications. *Computer methods in applied mechanics and engineering*, 139(1-4):289–314, 1996.
- [34] Yvan Notay. Convergence analysis of perturbed two-grid and multigrid methods. *SIAM journal on numerical analysis*, 45(3):1035–1044, 2007.
- [35] John W Ruge and Klaus Stüben. Algebraic multigrid. In *Multigrid methods*, pages 73–130. SIAM, 1987.
- [36] Jacob B Schroder. Smoothed aggregation solvers for anisotropic diffusion. *Numerical Linear Algebra with Applications*, 19(2):296–312, 2012.
- [37] Prateek Sharma and Gregory W Hammett. Preserving monotonicity in anisotropic diffusion. *Journal of Computational Physics*, 227(1):123–142, 2007.
- [38] Abdullah Ali Sivas, Ben S Southworth, and Sander Rhebergen. Air algebraic multigrid for a space-time hybridizable discontinuous galerkin discretization of advection (-diffusion). *SIAM Journal on Scientific Computing*, 43(5):A3393–A3416, 2021.
- [39] Carl R Sovinec, AH Glasser, TA Gianakon, DC Barnes, RA Nebel, SE Kruger, DD Schnack, SJ Plimpton, A Tarditi, MS Chu, et al. Nonlinear magnetohydrodynamics simulation using high-order finite elements. *Journal of Computational Physics*, 195(1):355–386, 2004.
- [40] Ulrich Trottenberg, Cornelius W Oosterlee, and Anton Schuller. *Multigrid*. Academic press, 2001.
- [41] Maria Vasilyeva. Generalized multiscale finite element method for discrete network (graph) models. *Journal of Computational and Applied Mathematics*, 457:116275, 2025.
- [42] Maria Vasilyeva, Valentin Alekseev, Eric T Chung, and Yalchin Efendiev. Multiscale dimension reduction for flow and transport problems in thin domain with reactive boundaries. *Journal of Computational Physics*, 442:110512, 2021.
- [43] Maria Vasilyeva, Masoud Babaei, Eric T Chung, and Valentin Alekseev. Upscaling of the single-phase flow and heat transport in fractured geothermal reservoirs using nonlocal multicontinuum method. *Computational Geosciences*, 23:745–759, 2019.
- [44] Maria Vasilyeva, Richard B Coffin, and Ingo Pecher. Decoupled multiscale numerical approach for reactive transport in marine sediment column. *Computer Methods in Applied Mechanics and Engineering*, 428:117087, 2024.

- [45] Maria Vasilyeva, Aashutosh Mistry, and Partha P Mukherjee. Multiscale model reduction for pore-scale simulation of li-ion batteries using gmsfem. *Journal of Computational and Applied Mathematics*, 344:73–88, 2018.
- [46] Maria Vasilyeva, Ben S Southworth, and Shubin Fu. An adaptive two-grid preconditioner for flow in fractured porous media. *arXiv preprint arXiv:2411.17903*, 2024.
- [47] Panayot S Vassilevski. *Multilevel block factorization preconditioners: Matrix-based analysis and algorithms for solving finite element equations*. Springer Science & Business Media, 2008.
- [48] Panayot S Vassilevski. Coarse spaces by algebraic multigrid: Multigrid convergence and upscaling error estimates. *Advances in Adaptive Data Analysis*, 3(01n02):229–249, 2011.
- [49] Pauli Virtanen, Ralf Gommers, Travis E Oliphant, Matt Haberland, Tyler Reddy, David Cournapeau, Evgeni Burovski, Pearu Peterson, Warren Weckesser, Jonathan Bright, et al. Scipy 1.0: fundamental algorithms for scientific computing in python. *Nature methods*, 17(3):261–272, 2020.
- [50] Golo A Wimmer, Ben S Southworth, Thomas J Gregory, and Xian-Zhu Tang. A fast algebraic multigrid solver and accurate discretization for highly anisotropic heat flux i: open field lines. *SIAM Journal on Scientific Computing*, 46(3):A1821–A1849, 2024.
- [51] Golo A Wimmer, Ben S Southworth, Koki Sagiya, and Xian-Zhu Tang. An accurate SUPG-stabilized continuous Galerkin discretization for anisotropic heat flux in magnetic confinement fusion. (*in review*), 2024.
- [52] Jinchao Xu and Ludmil Zikatanov. The method of alternating projections and the method of subspace corrections in hilbert space. *Journal of the American Mathematical Society*, 15(3):573–597, 2002.
- [53] Jinchao Xu and Ludmil Zikatanov. Algebraic multigrid methods. *Acta Numerica*, 26:591–721, 2017.